# 3R-TaS 2 as an Intercalation-Dependent Electrified Interface for Hydrogen Reduction and Oxidation Reactions

Hamid Ghorbani Shiraz, Zia Ullah Khan, Daniel Péré, Xianjie Liu, Yannick Coppel, Mats Fahlman, Magnus Berggren, Radoslaw Chmielowski, Myrtil Kahn, Mikhail Vagin, et al.

# 3R-$TaS_2$ as Intercalation-dependent Electrified Interface for Hydrogen Reduction and Oxidation Reactions

Hamid Ghorbani Shiraz[*1], Zia Ullah Khan[1], Daniel Péré[2], Xianjie Liu[1], Yannick Coppel[3], Mats Fahlman[1], Magnus Berggren[1], Radoslaw Chmielowski[2], Myrtil L. Kahn[3], Mikhail Vagin[*1], Xavier Crispin[1]

[1] Laboratory of Organic Electronics, Department of Science and Technology, Linköping University, Norrköping, SE-60174, Sweden.

[2] Department of Advanced Materials, IMRA Europe S.A.S., 06904 Sophia Antipolis, France.

[3] LCC-CNRS, University of Toulouse, CNRS, Toulouse, France.

Corresponding Author:
Hamid Gh. Shiraz – Hamid.ghorbani.shiraz@liu.se
Mikhail Vagin - mikhail.vagin@liu.se

## Abstract

The hydrogen technology, as a future breakthrough for energy industry, has been defined as an environmentally friendly, renewable, and high-power energy carrier. The green production of hydrogen, which majorly relays on electrocatalyst, is limited by the high cost and/or the performance of the catalytic system. Recently, studies have been conducted in search of a Bi-functional electrocatalysts accelerating both hydrogen evolution (HER) and hydrogen oxidation (HOR). Herein, we report the investigation of the high efficiency bi-functional electrocatalyst $TaS_2$ for both HER and HOR along with the asymmetric effect of inhibition by organic intercalation. The linear organic agent, to boost the electron donor property and to ease the process of intercalation, provides a higher interlayer gap in the tandem structure of utilized

nanosheets. XRD and XPS data reveals an increase of the interlayer distance by 22%. The HER and HOR were characterized in a Pt group metal-free electrochemical system. The pristine sample shows a low overpotential of - 0.016 V at onset. The intercalated sample demonstrates a large shift on its performance for HER. It is revealed that the intercalation is a potential key strategy for tuning the performance of this family of catalysts. The inhibition of HER by intercalation is considered as the increase of the operational window of water-based electrolyte on negative electrode, which is relevant to technologies of electrochemical energy storage.

**Introduction.** For many decades, hydrogen has been identified as a key energy carrier for a sustainable future society, as it offers a high energy density and principally no negative direct impact on the environment, with respect to $CO_2$ emissions. Hydrogen generation, as a first step towards a hydrogen economy, has been a matter of debate among scientists. Although many production methods, like photochemical or cracking reformation, or gasification of biomass, are being operated all over the world, there are several problems with current methods such as low yield or major environmental impacts.

One of the most efficient and clean processes to produce hydrogen is via electrochemical hydrogen evolution reaction (HER). There are many electrocatalysts for HER that possess high efficiencies, among which Pt, Rh, and Pd [1, 2] are commonly considered and explored. Although numerous candidates like hybrid structures (core-shell, alloys, composites, etc.) [3, 4], doped atom systems [5], metal organic frameworks [6], metal oxide arrays [7], etc. have shown proper performance characteristics, several major problems still lie ahead. Several studies are being conducted in the search for a cost-effective (especially targeting Platinum group metal-free catalysts), efficient, and scalable electrocatalyst. In that context, transition metal dichalcogenides (TMDs) constitute another class of two-dimensional materials where

the elemental periodic unit is composed of an atomic layer of a transition metal (Ti, Ta, Mo, W, etc.) in the center with a chalcogen atomic layer (S, Se) on either side. The geometry of chalcogen atoms with respect to transition metal results in various crystal structures (1T, 2H and 3R, etc.) where T, H and R represent overall structures (trigonal, hexagonal, and rhombohedral) and symmetry repetition is given with the number (1, 2, 3) of layers [8]. TMDs like $WS_2$ display significant activity for HER [9]. Also, $MoS_2$ is one of the most investigated TMDs towards HER [10-12]. Among TMDs, tantalum disulfide ($TaS_2$) exhibits the highest temperature-dependent electronic conductivity [13-15], which motivates the investigation of HER electrocatalytic activity of this 2D material for the use as (see Fig.1a and b). It is demonstrated that the majority of 2D structures are catalytically, several times more active at the edge sites, as compared to the basal plane [16]. To improve the (electro)catalytic activity, several modifications with the aim of activation of $TaS_2$ sheets are studied, such as plasma treatment [17], chemical exfoliation [18], atom-scale dispersion [19, 20], interfacial engineering, etc. Yu et al. have been using theoretical calculations that shows that cracked eight-awn star $TaS_2$ nanostructure possesses significant electrocatalytic properties [21]. They revealed that both basal and edge sites contribute to HER. Also, Hanlin et al. demonstrated that the electro-exfoliation of bulk $TaS_2$ into nanosheets can significantly enhance the electrocatalytic activity [22]; leading to low overpotential and a favorable Tafel slope of 197 mV (@10 $mA.cm^{-2}$) and 100 $mV.dec^{-1}$, respectively, while compared to those of the parent material (overpotential and Tafel slope of 547 mV and 216 $mV.dec^{-1}$, respectively). This demonstrates that the exfoliation of bulk $TaS_2$ can improve the performance, which may be ascribed to the increase of the interlayer space. Hence, nano-organization of the material is crucial, as it impacts the diffusion of protons via accommodation of more protons at the edge sites where the hot reaction sites are located.

Interestingly, $TaS_2$ can be exfoliated into nano-flakes, which can host a variety of linear and ring-shaped organic molecules in the inter-layer gaps (Fig. 1c). To the best of our knowledge, we have not found any prior study reporting the role of intercalated organic

molecule on the catalytic efficiency of the HER. In this work, we studied the effect of the intercalation of hexylamine (HA) in $TaS_2$ nanosheets on the HER performance. The exfoliated $TaS_2$ nanoflakes were studied with scanning electron microscopy (SEM) and their intercalation with the hexylamine was studied by X-ray diffraction (XRD). The surface compositions were analyzed with X-ray and UV-photoelectron spectroscopies (XPS, UPS). Additional evidence of the structure of the interaction between the organic molecules and exfoliated-$TaS_2$ were obtained by solid-state NMR spectroscopy and, finally, HER was measured in a standard electrochemical cell**.**

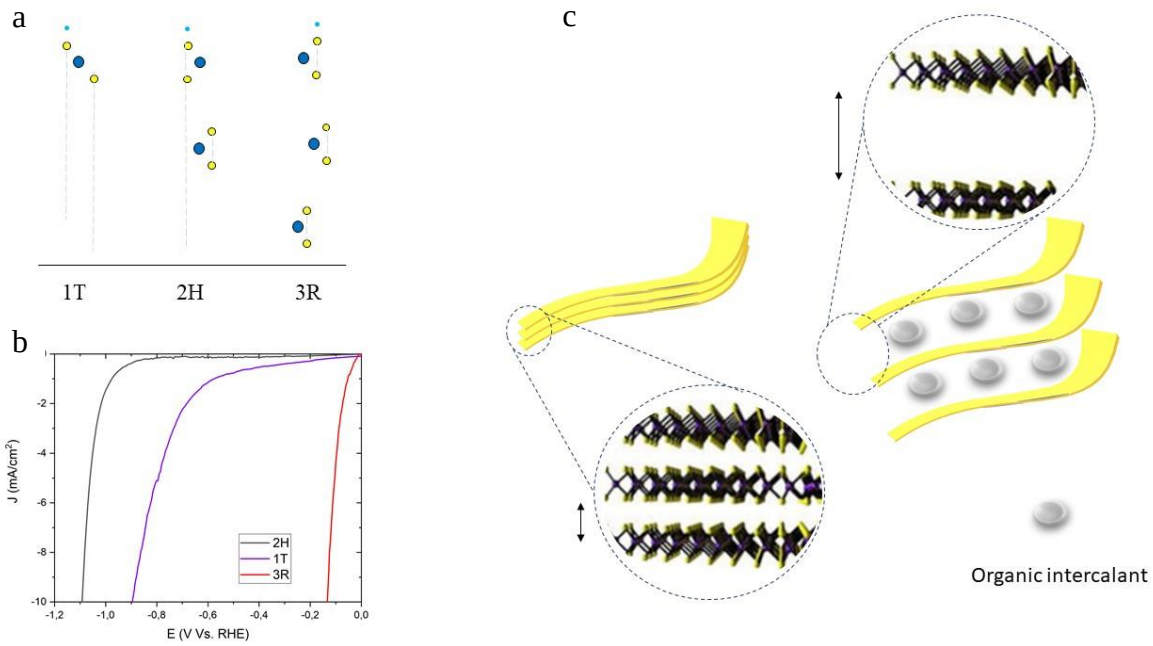


**Fig. 1:** (a) configuration of sulfurs (yellow) and Metal (dark blue) for different crystal phases, adsorbed with H atom (light blue); (b) high-efficiency HER electrocatalysis on 3R $TaS_2$; (c) intercalation of the pristine (stacked) nanosheets and increasing of the interlayer space.

**Methods**

**Material synthesis and ink formulation.** Tantalum (Ta) and Sulfur (S) powders were purchased from Goodfellow while hexylamine (HA) $C_6H_{15}N$ was bought from Sigma-Aldrich. Ta and S were mixed in stoichiometric ratio in an agate mortar and then transferred to quartz ampoule through a funnel. The ampoule was evacuated and flame-sealed. Later, it was placed in a vertical furnace for 48 hours at 900˚C and then quenched in water at room temperature. The ampoule was opened inside a $N_2$ glovebox, and the powder was passed through a 125 µm mesh. The powder was heated to 650 ˚C under vacuum to produce the 3R-$TaS_2$ crystal structure with an electrical conductivity (σ) of 500 S/cm. HA and $TaS_2$ were then mixed in 20:1 molar ratio inside a sealed glass bottle and stirred at 50 ˚C for 5 days. To suppress the agglomerated particles, the inks of the electrocatalysts were subjected to ultrasonication just before the casting of the films.

**Structural Characterization.** The X-ray diffraction patterns (XRD) were collected at room temperature using a D8 Bruker diffractometer equipped with a copper anode and a point detector. The scanning electron microscopy (SEM) investigations were carried out with a Hitachi S-4700 equipped with a field emission gun. For both XRD (Bruker D8 Advance / copper / theta-2theta mode / 5° - 67° / step 0.04° / time : 10s per step) and SEM (5.00 kV and 12.5*2.50k SE(M) and 10.0 kV and 13.2*5.00k SE(M) for top view and cross section images, respectively) analyses, the $TaS_2$ powders were drop-casted on glass substrates which were heated at 100˚C for 30 minutes inside glovebox to evaporate ethanol used as a solvent.

XPS/UPS (X-ray, ultraviolet photoemission spectroscopy) measurements have been performed in Scienta ESCA 200 system under the base pressure of 2E-10 mbar with SES 200 electron analyzer, a monochromatic Al Ka x-ray source ($h\upsilon$=1486.6 eV) and a helium discharge lamp ($h\upsilon$=21.22 eV) for XPS and UPS, respectively. All spectra were collected at normal emission and at room temperature. The spectrometer was calibrated by a sputter-

cleaned Au film with the Fermi level at 0 eV and Au 4f7/2 peak at 84.0 eV with its full width at half maximum being 0.65 eV for XPS. The total energy resolution of UPS is about 0.08 eV estimated from the width of the Fermi edge of a clean Au film. The work function of sample was extracted from the edge of the secondary electron cutoff in UPS spectrum with a bias of -3V applied in sample.

NMR experiments were recorded on Bruker Avance 400 III HD spectrometer operating at magnetic fields of 9.4 T. Samples were packed into 2.5 mm zirconia rotors under argon inside a glove box. The rotors were spun between 10 and 15 kHz at 295 K. $^{1}$H MAS were performed with the DEPTH pulse sequence and a recycle delay of 3 s. $^{13}$C MAS and CP-MAS were recorded with recycle delays of 5 s and 1.5 s, respectively and with a contact time of 2 ms for CP-MAS. Chemical shifts were externally referenced to liquid TMS. The NMR experiments had to be realized in small rotors (2.5 mm) because of the unfavorable electromagnetic properties of the samples.

**Electrochemical Characterization.** Electrochemical measurements were carried out using a three-electrode setup (BioLogic SP200 potentiostat) in 0.5 M $H_2SO_4$ solution. A graphite felt was used as a counter electrode to provide the highest possible surface area, and to avoid any metallic contamination [23]. The structure and performance of carbon felt characterized and proved during measurement. An Ag/AgCl and a rotating glassy carbon disk electrodes were used as a reference and working electrodes, respectively. A 5 wt% Nafion was used as a proton-conductive binder. The measurements were done in the electrolyte where the working electrode was rotating at 800 rpm and the system was purging using pure hydrogen gas. For analysis, all the potentials are converted to reversible hydrogen electrode using Nernst equation; in 0.5 M $H_2SO_4$ (pH=0) the equation is simplified as $E(RHE) = E(SCE) + 0.242$.

Linear sweep scan rate (LSV) curves were measured at the scan rate of 5 mV.sec$^{-1}$, in the range of 0.2 to -1 V versus RHE, all reported values are IR-compensated. The

electrochemical active surface area measurements were recorded at scan rates 10 to 500 $mV.sec^{-1}$ in a potential window of 0.14-0.24 (Vs. RHE).

**Results.** From the synthesis of $TaS_2$, we succeeded to obtain a powder of the 3R-$TaS_2$ crystal structure, which was supported by XRD studies. It was reported [24] that this structurally-controlled electrocatalyst showed a highest HER activity in comparison with the other $TaS_2$ crystal structures illustrated by the lowest overpotential for HER (0.2 V, compared to 0.47 V for 2H-$TaS_2$ and 0.55 V for 1T-$TaS_2$ and 0.02 V for Pt) and the lowest Tafel slope of 85 mV/dec (compared to 100 mV/dec for 2H-$TaS_2$, 155 mV/dec for 1T-$TaS_2$, and 30 mV/dec for Pt/C). The SEM image of the powder shows platelets of $TaS_2$ of various sizes (Fig. 2a). A compressed layer of this powder displays an electrical conductivity of 500 S/cm suggesting that it has a metallic character. To intercalate HA into the crystal strucutre, the following simple recipe was used: HA and the $TaS_2$ powder were mixed at a 20:1 molar ratio inside a sealed glass bottle and stirred at 50 ˚C for 5 days. That step results in the full intercalation of HA into partially exfoliated Ta $S_2$ nano-flakes.

After exfoliation and intercalation, the suspension was casted on top of a glass substrate to form a thin layer. SEM cross-section images, given in Fig. 2b, clearly indicates that the thin layers are formed of re-stacked exfoliated structures oriented parallel to the substrate.

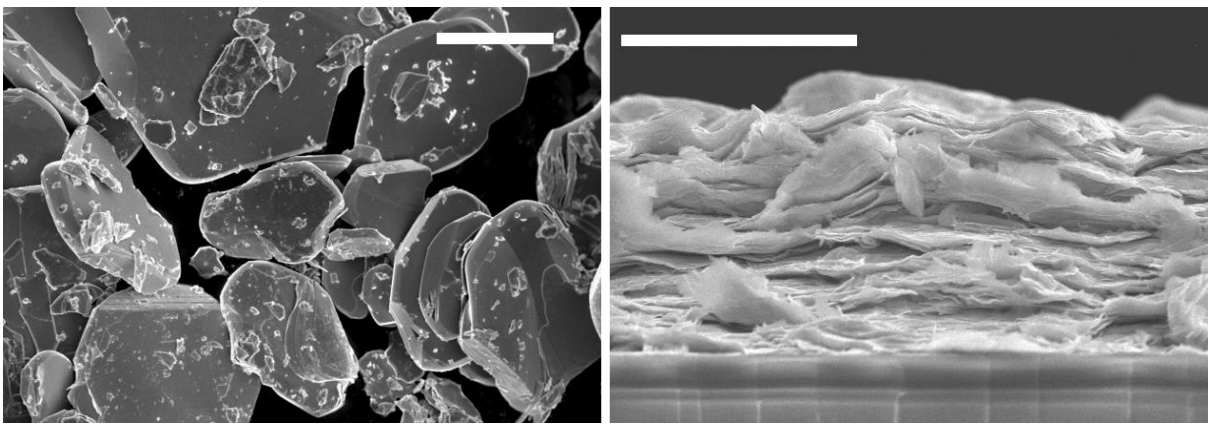

a b

c

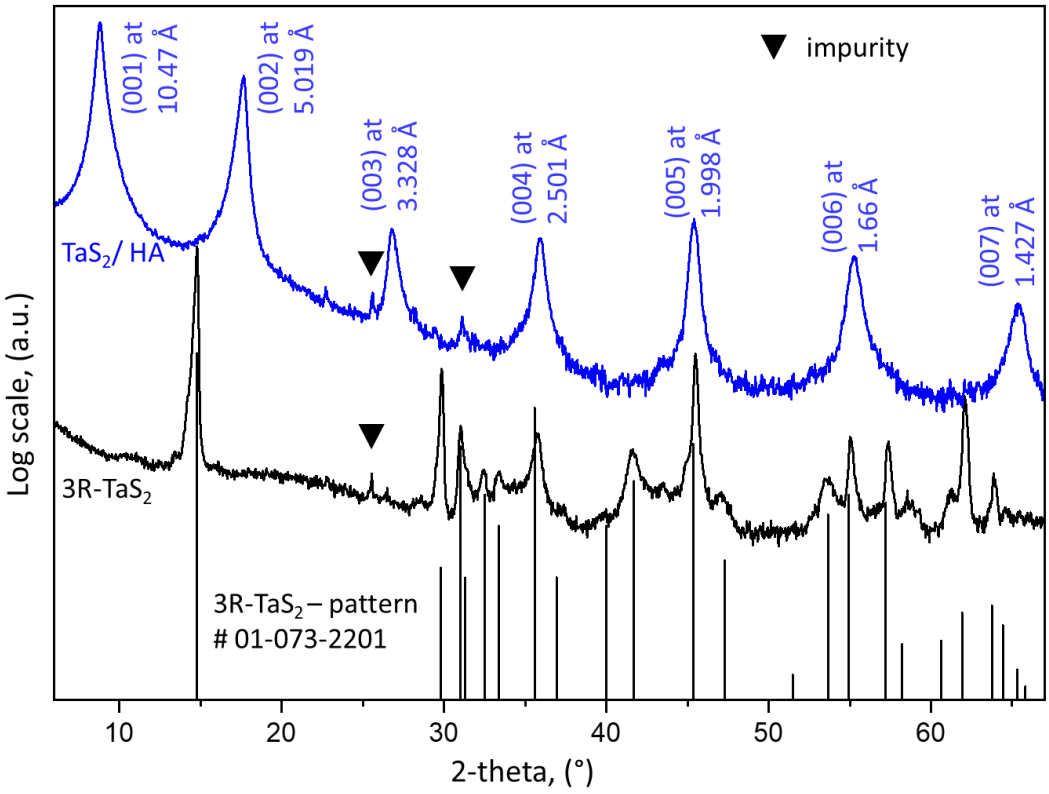


**Fig. 2:** SEM images of the $TaS_2$ (a) top view of the bulk powder; (b) cross-section of the film with $TaS_2$ and HA. The scale bar is 10 µm long. (c) XRD patterns collected on a pristine $TaS_2$ powder indexed with the 01-089-2756 (in black) and $TaS_2$ intercalated with hexylamine.

The X-ray diffraction patterns collected on pristine $TaS_2$ powder and $TaS_2$ intercalated with hexylamine are presented on figure 2c. The XRD pattern obtained from the drop-casted powder has the best match with the ICSD card 01-073-2201 [25] that corresponds to 3R-$TaS_2$ (black pattern). The intercalation of hexylamine into the 3R-$TaS_2$ leads to a superlattice of $TaS_2$/HA characterized by a series of (00$\ell$) peaks where $\ell$ = 1, 2 up to 7 (blue pattern). Beside strong diffraction from the superlative, some minor peaks are identified as impurity that could correspond to $TaO_x$. The comparison of both patterns indicates that the 3R-$TaS_2$ structure is completely modified by the intercalation of hexylamine as the diffraction from the 3R-$TaS_2$ is entirely vanished on the pattern of the $TaS_2$/HA.

To better understand the intercalation phenomenon of HA in 3R-$TaS_2$, the samples were analyzed by X-ray photoelectron spectroscopy (XPS). To emphasize the change on the valency and different chemical environments, all XPS data were plotted with the binding energy relative to the vacuum level. The Ta 4f spectrum of the pristine 3R-$TaS_2$ clearly indicated that there is more than one type of Ta valency (left panel in Fig. 3a). The doublet around 27 and 29 eV are from 3R-$TaS_2$, where the doublet around 30.5 and 32.5 eV can be attributed a surface oxide ($TaO_x$) [26] due to the exposure of 3R-$TaS_2$ to ambient air. Upon HA intercalation, the Ta4f doublet from the surface oxide $TaO_{5x}$ can be significantly decreased, which indicates that HA participates to the removal of the oxide. Also meanwhile, it can be clearly seen that the doublet from 3R-$TaS_2$ has a slight shift to the high binding energy, around 0.3 eV, compared to after HA intercalation. Both features indicate that there is electron transfer from HA to the surface oxide of 3R-$TaS_2$. Correspondingly, the spectral feature of S2p (right panel in Fig. 3b) from the pristine and HA-treated 3R-$TaS_2$ shows a decreasing intensity at the high binding energy contribution (ca. 168 eV) and a shift to the low binding energy (ca. 0.2 eV) after HA intercalation. The XPS data clearly indicates that there is a surface chemical reaction present; while the XRD proves that HA is fully intercalated.

a

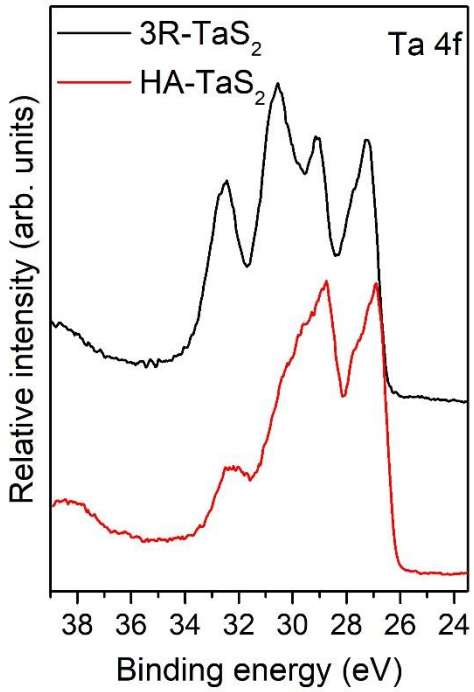
3R-TaS2
HA-TaS2
Ta 4f
Relative intensity (arb. units)
38 36 34 32 30 28 26 24
Binding energy (eV)

b

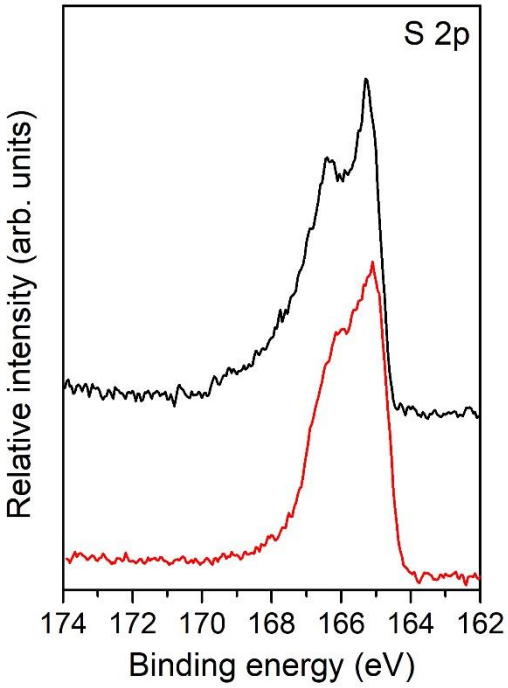
S 2p
Relative intensity (arb. units)
174 172 170 168 166 164 162
Binding energy (eV)

c

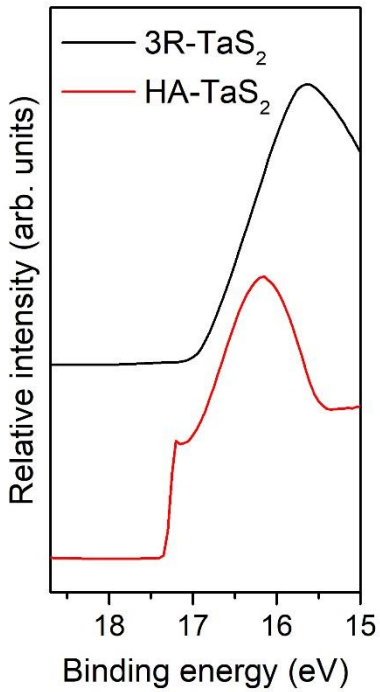
3R-TaS2
HA-TaS2
Relative intensity (arb. units)
18 17 16 15
Binding energy (eV)

d

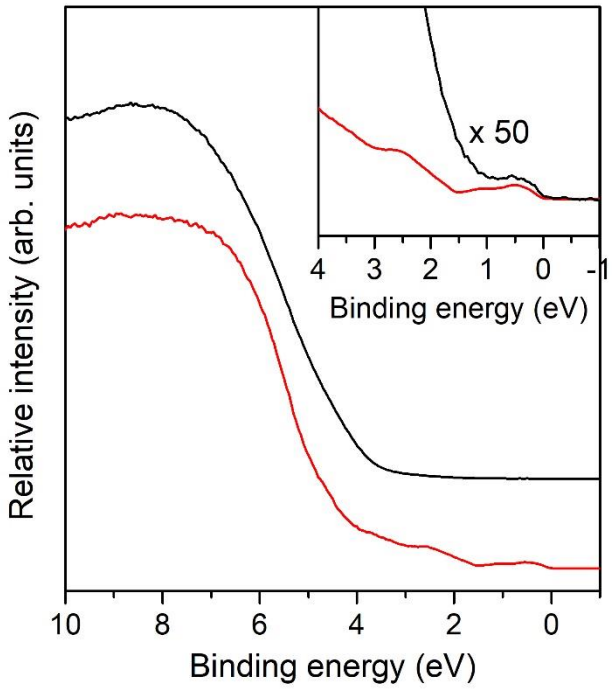
x 50
4 3 2 1 0 -1
Binding energy (eV)
Relative intensity (arb. units)
10 8 6 4 2 0
Binding energy (eV)

**Fig. 3:** Comparison of XPS spectra pristine and HA-intercalated samples; (a) Ta 4f and (b) S 2P. (c) and (d) are the second-electron cutoff and the UPS spectra of pristine and HA-intercalated $TaS_2$.

We pursuit the surface analysis by measuring the UV photoelectron spectra of the samples. A first observation is that the secondary electron cutoff of the UPS spectra (Fig. 3c) demonstrates that the work function of 3R-$TaS_2$ decreases from 4.3 eV, for the pristine air-exposed $TaS_2$ layer, to 3.9 eV after the intercalation of HA. The drop in work function by 0.4 eV indicates a significant change in the interfacial energetics. The most significant change of the UPS spectra upon HA intercalation is the appearance of the valence features of $TaS_2$ at 0.5 eV, 1.1 eV and 2.6 eV relative to the Fermi level (HA has a high valence band feature). On the contrary, there is no visible feature in the pristine 3R-$TaS_2$, and the spectral intensity is very low and there is almost featureless close to the Fermi level, which is mostly due to the presence of the insulating oxide surface layer with a large energy gap. The surface oxide $TaO_x$ has the dominant contribution to UPS spectrum of the 3R-$TaS_2$ surface. Indeed, by zooming in on the energy region close to the Fermi level (inset of Fig. 3d), the Fermi edge of the metallic $TaS_2$ is visible together with the first band at 0.5 eV on the pristine $TaS_2$ sample. The removal of the surface oxide by the HA treatment leads to an enhancement of about 50 times of the valence bands in addition to clear valance band features.

Further insight on the structure of HA interacting with exfoliated $TaS_2$ were obtained from solid-state NMR spectroscopy. Similar results were obtained regardless of the HA-functionalized $TaS_2$ batch suggesting that the synthesis is reliable and reproducible. $^1$H MAS spectrum of $TaS_2$ alone displays a weak and broad signal centered at 3 ppm that can be tentatively assigned to isolated hydroxyl groups and physisorbed water molecules (Fig 4a bottom). The $^1$H MAS spectrum of HA-intercalated $TaS_2$ (Fig. 4a top) shows stronger signals with a characteristic alkyl chain peak at 1.24 ppm and a shoulder at 7.24 ppm attributable to

ammonium. This assignment is confirmed by signal deconvolution (Fig. S2), with a ratio between the 7.24 and 1.24 signals equal to 0.18 (±0.03), that corresponds to the expected value of 0.2 (3/15, $(NH_3^+)/C_6H_{15}$) for the ammonium species. The $^{13}C$ CPMAS and MAS spectra (Fig. 4b) show broad peak characteristic of disordered structures. The alkylamines adopt several different conformations with varying coordination modes. The $^{13}C$ CPMAS and MAS spectra are very similar with a good sensitivity of the CP MAS experiment indicating that the amines are rigid in the material [27]. The position of the central $CH_2$ groups of the alkyl chain around 30 ppm indicates that the aliphatic chain of the amines is in the form of rigid pellets. Indeed, methylene C atoms with trans/gauche or gauche–gauche conformations exhibit signals at 29–31 ppm (γ-gauche effects) while for all-trans conformations, signals are observed at 33–34 ppm [28].

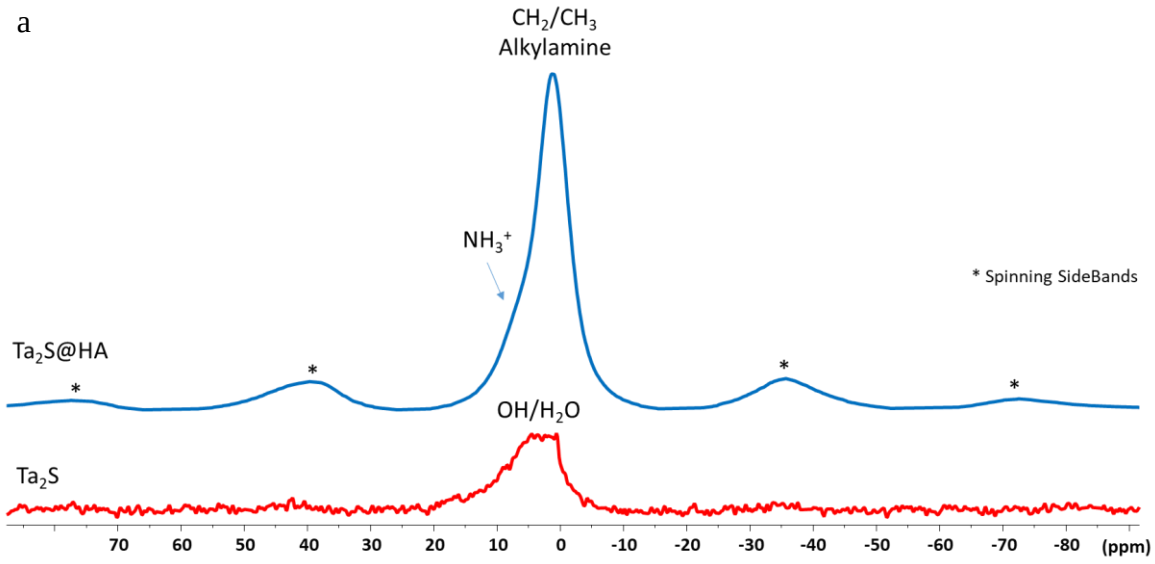

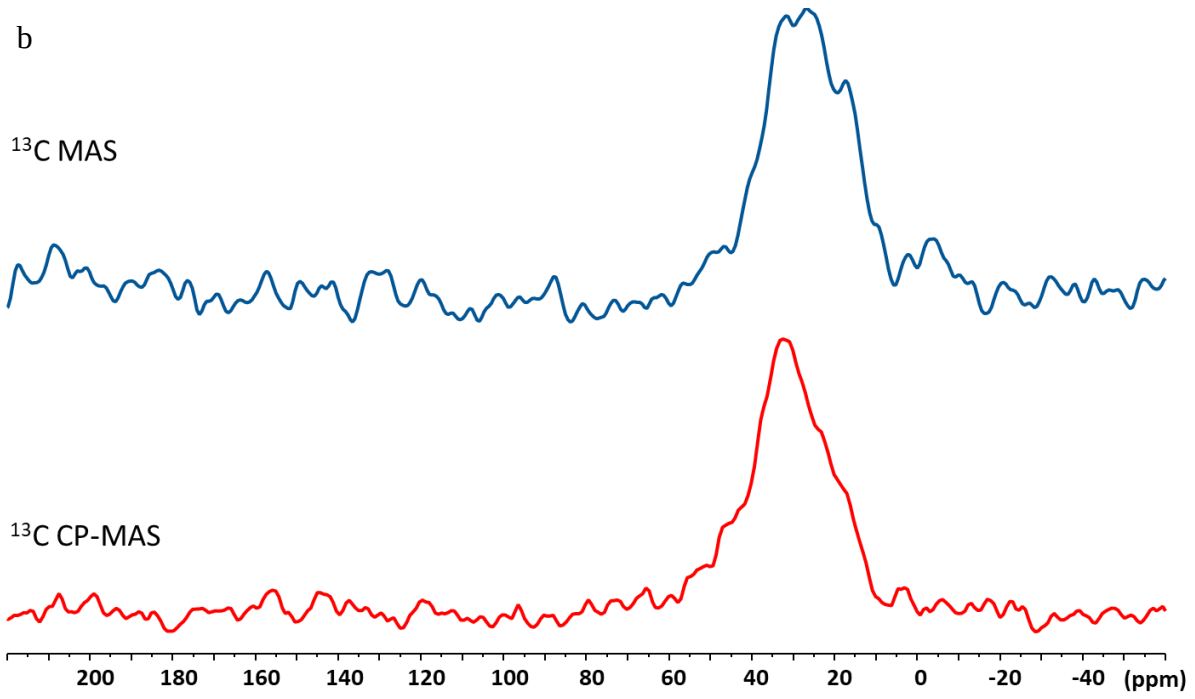


**Fig. 4:** a) $^{1}$H MAS spectrum of HA-intercalated $TaS_2$ and pristine $TaS_2$; a closer view clearly expresses the fingerprint of the ammonium species, see the deconvoluted spectra (Fig. S2); b) $^{13}$C CP MAS and $^{13}$C MAS spectra of HA-intercalated $TaS_2$.

Finally, we investigate the electrocatalytic performance of the $TaS_2$ with and without HA intercalation for both hydrogen evolution reaction (HER) and hydrogen oxidation reaction (HOR) in acidic medium. The electrode is prepared in the following way: the $TaS_2$ powder or the HA-$TaS_2$ nanoflakes are dispersed in an ethanol-water solution and mixed with 5wt% of Nafion as a binder, followed by a final deposition on a glassy carbon substrate. We have chosen the Nafion as the binder as it is not soluble in water and is also stable in acids. Moreover, it promotes the transport for protons inside the $TaS_2$ electrode layer, at humid/aqueous conditions. The linear sweep voltammetry visualizes a strong HER activity on the pristine 3R-$TaS_2$ (Fig. 5a). The potentials are referred to the zero-voltage corresponding to the thermodynamically dictated electronic energy threshold (reversible potential) of the reaction:

$$H^+ + e^- \leftrightarrow H^0 \qquad (1)$$

The zero voltage demarcates the potentials of HER and HOR manifested in reversible hydrogen electrode (RHE). The increase of electronic energy, which corresponds to the application of negative electric potential, beyond a threshold (so called overpotential) prioritizes the reaction (1) from left to right, *i.e.* the HER. The overpotential for our 3R-$TaS_2$/Nafion electrode is as low as 0.016 V at the onset. We speculate that the negatively charged Nafion might lead to small interfacial potential drop with respect to the electrolyte. So, the overpotential is very small and the HER-driven current rise is remarkable all through -70 mA $cm^{-2}$, at -0.08 mV, illustrating a diffusion-free behavior typical for fast proton transport. This impressive performance shows that the 3R-$TaS_2$/Nafion electrode is competitive with other state-of-the-art electrocatalysts for HER. In contrast, the HA-$TaS_2$/Nafion electrode with HA intercalation leads to a significantly higher overpotential to observe the onset of HER and a current level of -7 mA $cm^{-2}$ at -0.34 V, which is significantly smaller than with the $TaS_2$/Nafion electrode. Note that the blank current collector (glassy carbon) shows an overpotential of ca. 0.74 V, thus demonstrating that it has no impact on the current observed for the $TaS_2$-based electrodes deposited on glassy carbon.

The application-relevant steady-state measurements (Fig. 5b and 5c) confirm the increase HER rate on the $TaS_2$ electrode in comparison with HA intercalated electrode. Importantly, the steady-state measurements allow for the observation of HOR currents corresponding to the proceeding of the reaction (1) running from right to left. The data presentation in Tafel coordinates (Fig. 5c) enables us to investigate in detail the electrocatalytic phenomena of HER and HOR. In contrast to smooth glassy carbon electrode, both $TaS_2$-based electrodes showed non-monotonous dependence of current density on the overpotential of HER. Specifically, the region of current densities of 0.27 mA $cm^{-2}$ ($\ln(J) \sim -1.3$, Fig. 5c) is characterized with the change of the slope. This might illustrate the effect of kinetic limitation by the mass transport on the highly porous electrocatalyst. The low current densities enable the full involvement of the electrocatalyst surface distributed within nanoscale pores, while the

higher current densities are characterized by a limitation of reagent or product transport inside the pores. All electrode systems showed a Tafel slope of ca. 120 mV $dec^{-1}$. This implies that the rate-determining step in HER on all electrodes of this study is a Volmer step [29]:

$$H_3O^+ + e^- + M \leftrightarrow M \cdots H^0 + H_2O \quad (2).$$

where M denotes the surface empty site.

Coherently with linear sweep voltammetry measurements, HER showed a higher rate on pristine $TaS_2$ in comparison with the intercalated $TaS_2$. Interestingly, HOR current characteristics reveals an insensitivity to the effect of intercalation of HA in the $TaS_2$ electrodes. Note, however, that the HOR current is much higher than the vanishingly small current level of the glassy carbon collector. Both pristine and intercalated $TaS_2$-modified electrodes show a change of Tafel slopes from 40 mV $dec^{-1}$ to 120 mV $dec^{-1}$ as current densities increase. This corresponds to Volmer step as a rate-determining in HOR (reaction (2) proceeds from right to left) [29].

The extrapolation of Tafel slopes (120 mV $dec^{-1}$) for both HOR and HER yields the interception point corresponding to the exchange current density of HOR/HER – overpotential-free rate of the process, where the rates of both HOR and HER are equal. In order to take into account the effect of the nanoscale roughness of porous electrocatalysts [30], we normalized the estimated exchange current densities to the capacitive current densities, which are assumed to represent the electrochemically available surface area (EASA) of the electrode. The HA intercalated $TaS_2$ electrode shows up to 20 times higher capacitive currents as compared to the pristine material of the same mass load. We identified this difference as due to the exfoliation process taking place upon HA treatment while producing the nanoflakes (Fig. 2b). The exchange current densities estimated from the regions of small overpotentials were 0.041 mA $cm^{-2}$ ($\ln(J_0) \sim -3.18$) and 0.033 mA $cm^{-2}$ ($\ln(J_0) \sim -3.39$) for pristine and intercalated $TaS_2$. The exchange current densities estimated from the high overpotentials, featured with porous mass transport limitations, were 0.025 mA $cm^{-2}$ ($\ln(J_0) \sim -3.68$) and 0.021 mA $cm^{-2}$ ($\ln(J_0) \sim -3.87$)

for pristine and intercalated $TaS_2$, respectively. The exchange current density for blank glassy carbon is significantly smaller (0.0015 mA $cm^{-2}$ ($\ln(J_0) \sim -6.44$)). The kinetic characteristics obtained for $TaS_2$ are comparable with the rates of HER/HOR on gold (0.027 mA $cm^{-2}$ ($\ln(J_0) \sim -3.75$)) and significantly smaller than on platinum (0.78 mA $cm^{-2}$ ($\ln(J_0) \sim -0.23$)). The normalized exchanged current densities show a significant poisoning effect of the hexylamine intercalant (Table 1). The rate of HOR/HER on intercalated $TaS_2$ was more than 20 times smaller in comparison with pristine samples.

a

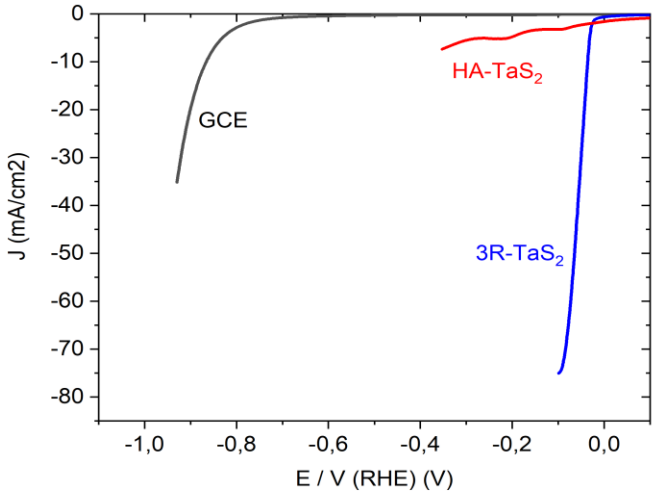
J (mA/cm2)
E / V (RHE) (V)
GCE
HA-TaS2
3R-TaS2

b

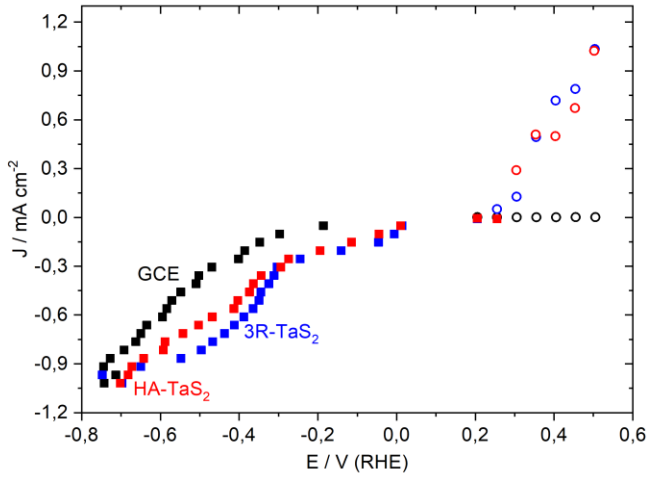
J / mA cm-2
E / V (RHE)
GCE
3R-TaS2
HA-TaS2

c

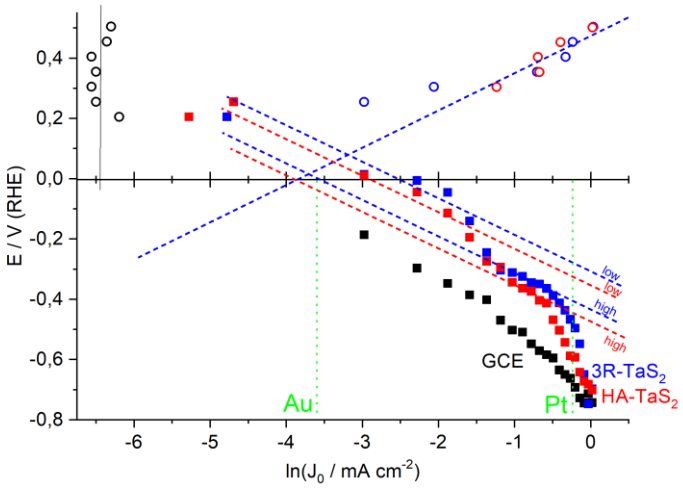
E / V (RHE)
ln(J0 / mA cm-2)
low
high
GCE
3R-TaS2
HA-TaS2
Au
Pt

**Fig. 5**. HER/HOR electrocatalysis on $TaS_2$. Linear sweep (a, 5 mV $s^{-1}$) and steady-state (b, waiting time of 5 minutes) voltammograms recorded on blank (■) and film-modified glassy carbon (pristine and intercalated $TaS_2$ as blue and red, respectively); (c) Tafel plot for the steady-state voltammetry data (filled and hollow symbols refer to HER and HOR, respectively; dashed lines – extrapolated Tafel regions); hydrogen-saturated 0.5 M $H_2SO_4$.

**Table 1. Kinetic parameters of HER/HOR on $TaS_2$.**

| **Interface** | | **$J_0$, mA $cm^{-2}$** | | **$J_0$ / $J_{capacitive}$** | |
|---|---|---|---|---|---|
| | | Small overpotentials | High overpotentials | Small overpotentials | High overpotentials |
| $TaS_2$ | Pristine | 0.041 | 0.025 | 0.041 | 0.025 |
| | Intercalated | 0.033 | 0.021 | 0.0016 | 0.0010 |
| Glassy carbon (Current collector) | | 0.0015 | | | |
| Gold [31] | | 0.027 | | | |
| Platinum [32] | | 0.78 | | | |

**Discussion.** To improve reaction rates, a critical phenomenon of interest is the removal/reduction/dissolution of the $Ta_2O_5$ surface oxide by the reaction with HA. Alkyl amines are known to serve as reducing agents for metal oxide nanoparticles [33], hence we believe that HA reduces $TaS_2$ to functionalize its surface (Fig. 6a) but also to remove the surface oxide of $TaS_2$. Both XPS and UPS results are in agreement with this interpretation. Now, the XRD demonstrates the full intercalation of the HA in the $TaS_2$, hence HA does not only remove the oxide but truly intercalates in the Van der walls gaps of the $TaS_2$. Understanding the nature of the surface and edge of the $TaS_2$ nanoflakes are important to explore the electrocatalytic reactions. The UPS reveals that the metallic electronic structure of $TaS_2$ (high density of states at the Fermi level) is enhanced after HA treatment as the surface oxide is removed. Thus, one could imagine that the electrocatalytic activity would be boosted thanks to available metallic levels on the surface. However, the electrochemical data tells us the opposite. Indeed, a larger overpotential and lower current densities are obtained for the HER upon HA intercalation. It is thus reasonable to think that the HA molecules are also forming sub-monolayer on the surface of the $TaS_2$ nano-flakes and that its interaction with Ta atoms blocks electrocatalytic reactions. For instance, it is known that HA is forming a monolayer on various 2D materials by a chemical reaction involving hydroxyl groups contaminating their surface in presence of air and humidity [34]. The mechanism proposed involves the basic character of the amine with a proton transfer from the surface hydroxide groups: $Ta\text{-}OH + H_2N\text{-}R \rightarrow (Ta\text{-}O^-)\ (^+NH_3\text{-}R)$ (See Fig. 6b). NMR spectroscopic measurements agree with this assumption. It is proved that the resulting formed monolayer can remove water molecules from the Van der walls gaps by expressing its hydrophobic character, which in turn suppresses the nanosheet catalytic activity and ion transport towards the HER. The structure of the aliphatic chain of HA in the form of rigid pellets also agreed with the hydrophobic character of the organic layer. The moderate water-blocking property is also demonstrated when similar architectures of graphene oxide is treated with different alkylamine [35]. Moreover, the contact angle of HA-treated $TaS_2$ nanoflakes is

twice of those measured on non-surface modified systems and further increases for longer alkyl chains of the alkylamine [36].

Apart from that, surface charges will remain at the surface of the structure, which gives that the zeta potential of the intercalated $TaS_2$ likely decreases. This decrement in surface charges has a detrimental effect on the electron transfer between the surface and the protons [36, 37]; thus, negatively impress the HER activity of the electrocatalyst.

Moreover, the intercalation with HA increases the band gap, meaning that the higher overpotential is needed to drive the reaction of hydrogen reduction [38]. In principle, the HA intercalation will increase the interlayer gap between nanosheets.

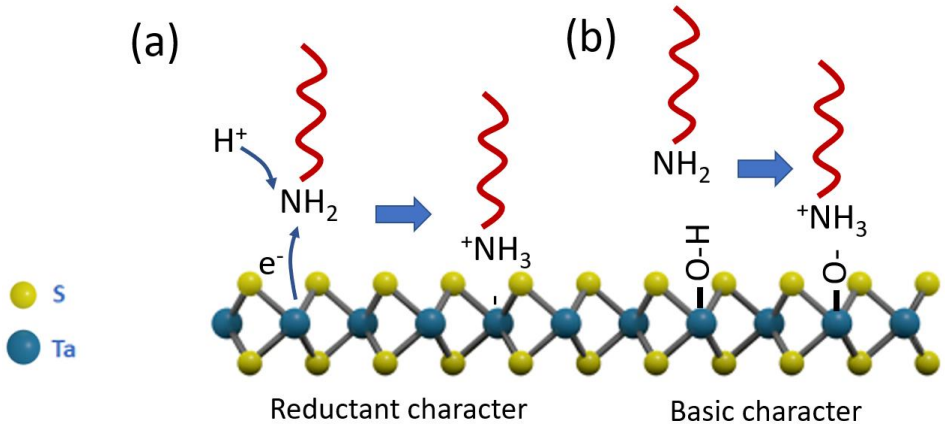

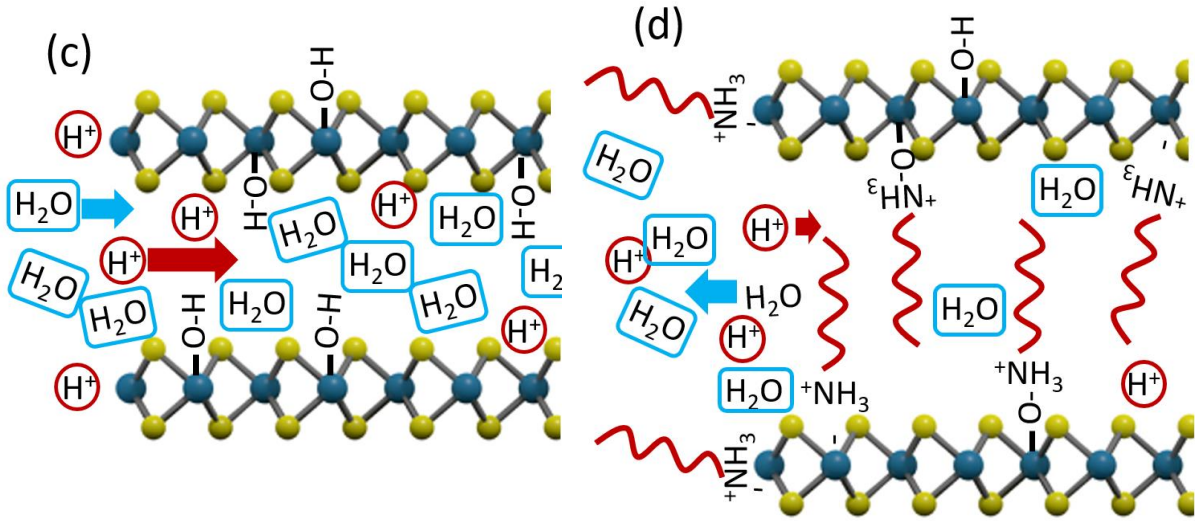


**Fig. 6**. (a) reductant character of the hexylamine leading to electron transfer and chemical interaction with $TaS_2$. (b) Basic character of the hexylamine reacting with a hydroxyl surface group on $TaS_2$. (c) Proton diffusion is promoted in the hydrophilic Van der walls gaps of the $TaS_2$. (d) hexylamine intercalation of $TaS_2$ leads to hydrophobic Van der walls gaps that blocks the water diffusion and diminish the transport of proton to catalytic sites.

However, the effect of impurity was not inevitable in this study, as the impurity is detected by XRD spectrum (Fig. 2). We assume that we have some impurity during the synthesis of electrocatalyst, since the materials were transferred to ampoule and later passed through a mesh. These introduces impurities and possible defects to the film, which may impact the performance of electrocatalysts [39, 40]. The optimized effect of defects might enhance the performance of electrocatalyst, though, as it is already reported in case of transitional metal dichalcogenide HER application [41]. The reason is that the optimized level of defects can offer local higher charge density [42]. Although there are some reports regarding the one-spot electrodeposition directly on electrode [40], the side deposition of species is not inevitable.

**Conclusions.** In summary, 3R-$TaS_2$ nanosheets and the hexylamine-treated derivative were investigated for hydrogen evolution. Aliphatic intercalant can conduct a high electron donor process of intercalation. XPS and XRD spectroscopy measurements shows that the interlayer distance in nanosheets has been increased as a result of hexylamine intercalation. Polarization curves show us an excellent performance of the pristine 3R-$TaS_2$ sample, while the intercalated sample reveals a deteriorated performance. The suppressing effect of HA-$TaS_2$ could be arisen from the i) decrease of the surface charges associated to a decrease of their mobility, ii) water molecule-blocking, and iii) bandgap increment, as post-intercalation effects. Apart from that, the hydrogen oxidation measurements express that both catalysts are quite active for the reverse reaction when hydrogen is oxidized, converted to electricity. While the current density for catalyst are exponentially increases as potential increases, glassy carbon doesn't show any potential dependency and stays at current density of 0 V. Tafel slopes also show the Volmer reaction as the rate determining step for both evolution and oxidation of hydrogen. This work demonstrates $TaS_2$ nanosheets as versatile electrified interface, which can be used either as efficient HER/HOR electrocatalyst or as an inert current collector.

## Supporting Information

Cyclic Voltammograms, $^1$H MAS


## Acknowledgments

This work was financially supported by the Swedish Research Council (VR 2016-05990), the Knut and Alice Wallenberg Foundation (KAW 2019.0604; 2021.0195), Karl Erik Önnesjös Foundation, and the Swedish Government Strategic Research Area in Materials Science on Advanced Functional Materials at Linköping University (Faculty Grant SFO-Mat-LiU No. 2009-00971).

## References

(1) Jin, T. L.; Liu, X.; Wang, H.; Wu, X.; Zhang, Y., Mechanochemical-Assisted Synthesis of Ternary Ru-Ni-S Pyrite Analogue for Enhanced Hydrogen Evolution Performance. *Carbon* **2020**, *162*, 172-180.

(2) Suliman, M. H.; Adam, A.; Li, L.; Tian, Z.; Siddiqui, M. N.; Yamani, Z. H.; Qamar, M., Fep/Mos2 Enriched with Dense Catalytic Sites and High Electrical Conductivity for the Hydrogen Evolution Reaction. *ACS Sustainable Chemistry & Engineering* **2019**, *7*, 17671-17681.

(3) Bai, S.; Wang, C.; Deng, M.; Gong, M.; Bai, Y.; Jiang, J.; Xiong, Y., Surface Polarization Matters: Enhancing the Hydrogen-Evolution Reaction by Shrinking Pt Shells in Pt–Pd–Graphene Stack Structures. *Angewandte Chemie* **2014**, *126*, 12316-12320.

(4) Yan, X.; Tian, L.; He, M.; Chen, X., Three-Dimensional Crystalline/Amorphous Co/Co3o4 Core/Shell Nanosheets as Efficient Electrocatalysts for the Hydrogen Evolution Reaction. *Nano letters* **2015**, *15*, 6015-6021.

(5) Luo, X.; Zhou, Q.; Du, S.; Li, J.; Zhang, L.; Lin, K.; Li, H.; Chen, B.; Wu, T.; Chen, D., One-Dimensional Porous Hybrid Structure of Mo2c-Cop Encapsulated in N-Doped Carbon Derived from Mof: An Efficient Electrocatalyst for Hydrogen Evolution Reaction over the Entire Ph Range. *ACS Applied Materials & Interfaces* **2018**, *10*, 42335-42347.

(6) Lin, Y.; Zhang, M.; Zhao, L.; Wang, L.; Cao, D.; Gong, Y., Ru Doped Bimetallic Phosphide Derived from 2d Metal Organic Framework as Active and Robust Electrocatalyst for Water Splitting. *Applied Surface Science* **2021**, *536*, 147952.

(7) Zhu, Y.; Lin, Q.; Zhong, Y.; Tahini, H. A.; Shao, Z.; Wang, H., Metal Oxide-Based Materials as an Emerging Family of Hydrogen Evolution Electrocatalysts. *Energy & Environmental Science* **2020**, *13*, 3361-3392.

(8) Dunnill, C. W.; MacLaren, I.; Gregory, D. H., Superconducting Tantalum Disulfide Nanotapes; Growth, Structure and Stoichiometry. *Nanoscale* **2010**, *2*, 90-97.

(9) Geng, S.; Yang, W.; Liu, Y.; Yu, Y., Engineering Sulfur Vacancies in Basal Plane of Mos2 for Enhanced Hydrogen Evolution Reaction. *Journal of Catalysis* **2020**, *391*, 91-97.

(10) Voiry, D.; Salehi, M.; Silva, R.; Fujita, T.; Chen, M.; Asefa, T.; Shenoy, V. B.; Eda, G.; Chhowalla, M., Conducting Mos2 Nanosheets as Catalysts for Hydrogen Evolution Reaction. *Nano letters* **2013**, *13*, 6222-6227.

(11) Li, Y.; Wang, H.; Xie, L.; Liang, Y.; Hong, G.; Dai, H., Mos2 Nanoparticles Grown on Graphene: An Advanced Catalyst for the Hydrogen Evolution Reaction. *Journal of the American Chemical Society* **2011**, *133*, 7296-7299.
(12) Yu, Y.; Huang, S.-Y.; Li, Y.; Steinmann, S. N.; Yang, W.; Cao, L., Layer-Dependent Electrocatalysis of Mos2 for Hydrogen Evolution. *Nano letters* **2014**, *14*, 553-558.
(13) Bulaevskiĭ, L., Structural Transitions with Formation of Charge-Density Waves in Layer Compounds. *Soviet Physics Uspekhi* **1976**, *19*, 836.
(14) Gamble, F.; Osiecki, J. H.; Cais, M.; Pisharody, R.; DiSalvo, F.; Geballe, T., Intercalation Complexes of Lewis Bases and Layered Sulfides: A Large Class of New Superconductors. *Science* **1971**, *174*, 493-497.
(15) Gamble, F.; DiSalvo, F.; Klemm, R.; Geballe, T., Superconductivity in Layered Structure Organometallic Crystals. *Science* **1970**, *168*, 568-570.
(16) Zhang, X.; Fei, H.; Wu, Z.; Wang, D., A Facile Preparation of Ws2 Nanosheets as a Highly Effective Her Catalyst. *Tungsten* **2019**, *1*, 101-109.
(17) Li, H.; Tan, Y.; Liu, P.; Guo, C.; Luo, M.; Han, J.; Lin, T.; Huang, F.; Chen, M., Atomic-Sized Pores Enhanced Electrocatalysis of Tas2 Nanosheets for Hydrogen Evolution. *Advanced Materials* **2016**, *28*, 8945-8949.
(18) Wu, J.; Liu, M.; Chatterjee, K.; Hackenberg, K. P.; Shen, J.; Zou, X.; Yan, Y.; Gu, J.; Yang, Y.; Lou, J., Exfoliated 2d Transition Metal Disulfides for Enhanced Electrocatalysis of Oxygen Evolution Reaction in Acidic Medium. *Advanced Materials Interfaces* **2016**, *3*, 1500669.
(19) Wang, X.; Wang, D.; Lu, Y.; Song, C.; Pan, J.; Li, C.; Sui, M.; Zhao, W.; Huang, F. In *Atom-Scale Dispersed Palladium in a Conductivepd0. 1tas2 Lattice with a Unique Electronic Structurefor Efficient Hydrogen Evolution*, ECS Meeting Abstracts, IOP Publishing: 2020; p 2434.
(20) Yu, Q.; Luo, Y.; Qiu, S.; Li, Q.; Cai, Z.; Zhang, Z.; Liu, J.; Sun, C.; Liu, B., Tuning the Hydrogen Evolution Performance of Metallic 2d Tantalum Disulfide by Interfacial Engineering. *ACS nano* **2019**, *13*, 11874-11881.
(21) Feng, Y.; Yu, K.; Zhu, Z., Cracked Eight-Awn Star Tas 2 with Fractal Structures Used as an Efficient Electrocatalyst for the Hydrogen Evolution Reaction. *CrystEngComm* **2019**, *21*, 3517-3524.
(22) Chen, H.; Si, J.; Lyu, S.; Zhang, T.; Li, Z.; Lei, C.; Lei, L.; Yuan, C.; Yang, B.; Gao, L., Highly Effective Electrochemical Exfoliation of Ultrathin Tantalum Disulfide Nanosheets for

Energy-Efficient Hydrogen Evolution Electrocatalysis. *ACS applied materials & interfaces* **2020**, *12*, 24675-24682.

(23) Gu, C.; Norris, B. C.; Fan, F.-R. F.; Bielawski, C. W.; Bard, A. J., Is Base-Inhibited Vapor Phase Polymerized Pedot an Electrocatalyst for the Hydrogen Evolution Reaction? Exploring Substrate Effects, Including Pt Contaminated Au. *ACS Catalysis* **2012**, *2*, 746-750.

(24) Feng, Y.; Gong, S.; Du, E.; Chen, X.; Qi, R.; Yu, K.; Zhu, Z., 3r Tas2 Surpasses the Corresponding 1t and 2h Phases for the Hydrogen Evolution Reaction. *The Journal of Physical Chemistry C* **2018**, *122*, 2382-2390.

(25) Bevan, D.; Martin, R. L.; Vegas, A., Rationalization of the Substructures Derived from the Three Fluorite-Related [Li6 (Mvli) N4] Polymorphs: An Analysis in Terms of the "Bärnighausen Trees" and of the "Extended Zintl–Klemm Concept". In *Inorganic 3d Structures*, Springer: 2011; pp 93-131.

(26) Chamlagain, B.; Cui, Q.; Paudel, S.; Cheng, M. M.-C.; Chen, P.-Y.; Zhou, Z., Thermally Oxidized 2d Tas2 as a High-K Gate Dielectric for Mos2 Field-Effect Transistors. *2D Materials* **2017**, *4*, 031002.

(27) Spataro, G.; Champouret, Y.; Coppel, Y.; Kahn, M. L., Prominence of the Instability of a Stabilizing Agent in the Changes in Physical State of a Hybrid Nanomaterial. *ChemPhysChem* **2020**, *21*, 2454-2459.

(28) Spataro, G.; Champouret, Y.; Florian, P.; Coppel, Y.; Kahn, M. L., Multinuclear Solid-State Nmr Study: A Powerful Tool for Understanding the Structure of Zno Hybrid Nanoparticles. *Physical Chemistry Chemical Physics* **2018**, *20*, 12413-12421.

(29) Shinagawa, T.; Garcia-Esparza, A. T.; Takanabe, K., Insight on Tafel Slopes from a Microkinetic Analysis of Aqueous Electrocatalysis for Energy Conversion. *Scientific reports* **2015**, *5*, 1-21.

(30) Voiry, D.; Chhowalla, M.; Gogotsi, Y.; Kotov, N. A.; Li, Y.; Penner, R. M.; Schaak, R. E.; Weiss, P. S., Best Practices for Reporting Electrocatalytic Performance of Nanomaterials. ACS Publications: 2018; Vol. 12, pp 9635-9638.

(31) Creţu, R.; Kellenberger, A.; Medeleanu, M.; Vaszilcsin, N., Cathodic Hydrogen Evolution Reaction on Gold Catalyzed by Proton-Carriers. *Int. J. Electrochem. Sci* **2014**, *9*, 4465-4477.

(32) Nørskov, J. K.; Bligaard, T.; Logadottir, A.; Kitchin, J.; Chen, J. G.; Pandelov, S.; Stimming, U., Trends in the Exchange Current for Hydrogen Evolution. *Journal of The Electrochemical Society* **2005**, *152*, J23.

(33) Meffre, A.; Lachaize, S.; Gatel, C.; Respaud, M.; Chaudret, B., Use of Long Chain Amine as a Reducing Agent for the Synthesis of High Quality Monodisperse Iron (0) Nanoparticles. *Journal of Materials Chemistry* **2011**, *21*, 13464-13469.

(34) Su, C.; Yin, Z.; Yan, Q.-B.; Wang, Z.; Lin, H.; Sun, L.; Xu, W.; Yamada, T.; Ji, X.; Zettsu, N., Waterproof Molecular Monolayers Stabilize 2d Materials. *Proceedings of the National Academy of Sciences* **2019**, *116*, 20844-20849.

(35) Abdullahi, B.; Ahmed, E.; Al Abdulgader, H.; Alghunaimi, F.; Saleh, T. A., Facile Fabrication of Hydrophobic Alkylamine Intercalated Graphene Oxide as Absorbent for Highly Effective Oil-Water Separation. *Journal of Molecular Liquids* **2021**, *325*, 115057.

(36) Huang, W.-M.; Liao, W.-S.; Lai, Y.-M.; Chen, I.-W. P., Tuning the Surface Charge Density of Exfoliated Thin Molybdenum Disulfide Sheets Via Non-Covalent Functionalization for Promoting Hydrogen Evolution Reaction. *Journal of Materials Chemistry C* **2020**, *8*, 510-517.

(37) Shiraz, H. G.; Crispin, X.; Berggren, M., Transition Metal Sulfides for Electrochemical Hydrogen Evolution. *International Journal of Hydrogen Energy* **2021**, *46*, 24060-24077.

(38) Hunt, A.; Kurmaev, E.; Moewes, A., Band Gap Engineering of Graphene Oxide by Chemical Modification. *Carbon* **2014**, *75*, 366-371.

(39) Toh, R. J.; Sofer, Z.; Luxa, J.; Pumera, M., Ultrapure Molybdenum Disulfide Shows Enhanced Catalysis for Hydrogen Evolution over Impurities-Doped Counterpart. *ChemCatChem* **2017**, *9*, 1168-1171.

(40) Strange, L. E.; Garg, S.; Kung, P.; Ashaduzzaman, M.; Szulczewski, G.; Pan, S., Electrodeposited Transition Metal Dichalcogenides for Use in Hydrogen Evolution Electrocatalysts. *Journal of The Electrochemical Society* **2022**, *169*, 026510.

(41) Wang, J.; Liu, J.; Zhang, B.; Ji, X.; Xu, K.; Chen, C.; Miao, L.; Jiang, J., The Mechanism of Hydrogen Adsorption on Transition Metal Dichalcogenides as Hydrogen Evolution Reaction Catalyst. *Physical Chemistry Chemical Physics* **2017**, *19*, 10125-10132.

(42) Jia, Y.; Zhang, L.; Gao, G.; Chen, H.; Wang, B.; Zhou, J.; Soo, M. T.; Hong, M.; Yan, X.; Qian, G., A Heterostructure Coupling of Exfoliated Ni–Fe Hydroxide Nanosheet and Defective Graphene as a Bifunctional Electrocatalyst for Overall Water Splitting. *Advanced Materials* **2017**, *29*, 1700017.

**TOC Graphic**